Electronic Supplementary Material (ESI) for Materials Horizons.

Supplementary Information

The Energy Landscape Governs Ductility in Disordered Materials

Longwen Tang,[1, 2] Han Liu,[2] Gang Ma,[1] Tao Du,[2,3] Normand Mousseau,[4] Wei Zhou,[1]* Mathieu Bauchy[2]*

[1] State Key Laboratory of Water Resources and Hydropower Engineering Science, Wuhan University, Wuhan 430072, China.

[2] Physics of AmoRphous and Inorganic Solids Laboratory (PARISlab), Department of Civil and Environmental Engineering, University of California, Los Angeles, California 90095, USA.

[3] Key Lab of Structures Dynamic Behavior and Control of the Ministry of Education, Harbin Institute of Technology, Harbin 150090, China.

[4] Département de Physique and Regroupement Québécois sur les Matériaux de Pointe,Université de Montréal, Case Postale 6128, Succursale Centre-Ville, Montréal (QC), Canada H3C 3J7.

Corresponding author: zw_mxx@whu.edu.cn
bauchy@ucla.edu

Mode I fracture simulations

We simulate a series of athermal and quasistatic uniaxial tension tests for various disordered systems. As illustrated in Fig. S1, we iteratively impose small increments of strain in the *z* direction, while the lateral dimensions of the simulation box (*x* and *y* directions) are fixed during the loading process. Then, after each increment of strain, an energy minimization is performed by using the conjugate gradient algorithm. The above steps are repeated until a complete fracture is observed. This procedure is equivalent to relaxing the system under *NVT* ensemble at 0 K for enough time after each strain increment.

Crystallization of the LJ system

In the following, all the results are given in reduced units, that is, length in units of σ, energy in units of ε, stress in units of ε/σ^3, time in units of $\tau = \sigma(m/\varepsilon)^{1/2}$ (where $m =$ 1.0 is the mass of particles), etc. The monodisperse LJ system considered herein is more likely to crystallize than polydisperse LJ systems. However, this system is still stable enough to remain disordered over extended durations (i.e., over typical MD times of $10^3\tau$) if the temperature is low enough. To quantity the range of temperature and time over which the system can avoid crystallization, we conducted a series of additional MD simulations to determine the time after which the system crystalizes as a function of temperature. This is accomplished by heating the system up to a target temperature and relaxing it under zero pressure in the *NPT* ensemble until crystallization is observed (which manifests itself by a sudden drop in potential energy, see Fig. S2a, and a sharpening of the pair distribution peaks). As shown in Fig. S2b, this analysis yields a typical TTT curve, wherein the system avoids crystallization at high temperature (due to the absence of any thermodynamic driving force) and low temperature (due to a slow kinetics). In turn, the "nose" of the TTT curve at intermediate temperature provides the range of time over which the system can resist crystallization (so that the monodisperse LJ model considered herein can be applied).

We observe that, although the monodisperse LJ model may not be suitable to model atomic glasses (e.g., metallic glasses), it can properly describe a wide variety of disordered materials (gels, colloids, and granular materials) for which the unit energy ε is high enough, so that 300 K corresponds to a reduced temperature for which no crystallization is observed.

To illustrate that the results presented in the main manuscript remain valid at finite temperature, we repeated our analysis at non-zero temperature by taking as an example a hydrated silicate colloidal gel at 300 K. As shown in Fig. S3, we observe that, indeed, the power law relationship between cumulative non-affine displacement and minimum energy barrier holds at non-zero temperature—which demonstrates the generality of our findings.

Cumulative non-affine displacement

Note that this definition differs from that of the total non-affine displacement (as obtained by comparing the initial and final configurations) since, here, the non-affine displacement is always calculated by comparing two configurations that are fairly close to each other (i.e., separated from each other by only a small increment of strain). The difference between the cumulative non-affine displacement (as used herein) and the total non-affine displacement is illustrated in Fig. S4(a) in the case of a perfectly brittle fracture, wherein the top blue particles move upward as a rigid body, whereas the bottom red particles move down as a rigid body. Since the total non-affine displacement D^2_{min} only considers the initial and final configurations, the total non-affine displacement does not properly capture the local ductile events (or absence thereof herein) as it continually increases. In contrast, the cumulative non-affine displacement D used herein does not show any increase once the fracture has occurred. To further illustrate this difference, Fig. S4(b) and Fig. S4C show the evolution of the $\Delta D_{i,\mathrm{min}}$, D^2_{min} , and D metrics of a select given particle as a function of strain during the fracture of a silicate gel system. We find that all the plastic events undergone by this particle manifest themselves as a peak in $\Delta D_{i,\mathrm{min}}$, which, in turn, results in a discontinuity in D. The fact that a given particle can experience several distinct non-affine plastic displacements during the fracture process eventually leads to a non-meaningful evolution of D^2_{min} , which tends to continuously increase (Fig. S4(c)). In contrast, the metric D used in this paper can meaningfully capture the number and magnitude of the local plastic events occurring within the atomic network during the fracture process.

Mechanical energy

To assess whether or not the energy barriers presented in Fig. 3 can be activated by the stress resulting from the deformation, we calculate the mechanical energy resulting from the imposed deformation $E_{\mathrm{m}}(\varepsilon) = V \int_0^{\varepsilon} \sigma d\varepsilon$, where V is the volume of system. As shown in Fig. S6, the mechanical energy observed in the colloidal gels is notably larger than in the case of glassy silica—mostly on account of their larger volume. Importantly, in both cases, the resulting mechanical energy is large enough to overcome the energy barriers shown in Fig. 3.

Silica glass with various cooling rates

To generate silica glasses with different cooling rates, we first melt the irradiated silica system at 5000 K under zero pressure in the *NPT* ensemble for 1 ns, which ensures that the system loses the memory of its initial configuration. The melt is then subsequently cooled down to 1 K with different cooling rate (i.e., 1 K/ps and 100 K/ps) under zero pressure in the *NPT* ensemble. Finally, the obtained glasses are relaxed at 1 K and under zero pressure for an additional 1 ns. The obtained glasses are subjected to uniaxial tensile deformations using the method described above.

As shown in Fig. S11, the fast-quenched glass (i.e., more disordered system) shows a more ductile fracture behavior as compared to the slowly-quenched glass (i.e., less disordered system)—which echoes results obtained for irradiated samples. Importantly, we find that the relationship between plastic energy and non-affine particle displacement in these melt-quenched systems follows the same trend as the one observed in the irradiated systems (see the inset of Fig. S11a). This suggests that the origin of structural disorder (i.e., induced by melt-quenching or irradiation) does not appear to notably impact the nature of relationship between ductility and particle dynamics. In addition, we observe that the power law relationship between D and E_{ave} observed in irradiated systems still holds in melt-quenched glasses.

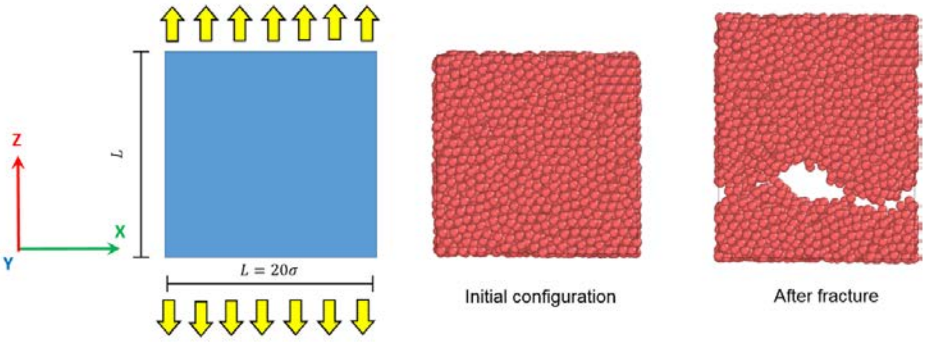

Fig. S1. Schematic describing the geometry of a disordered structure subjected to uniaxial tension under athermal and quasistatic conditions.

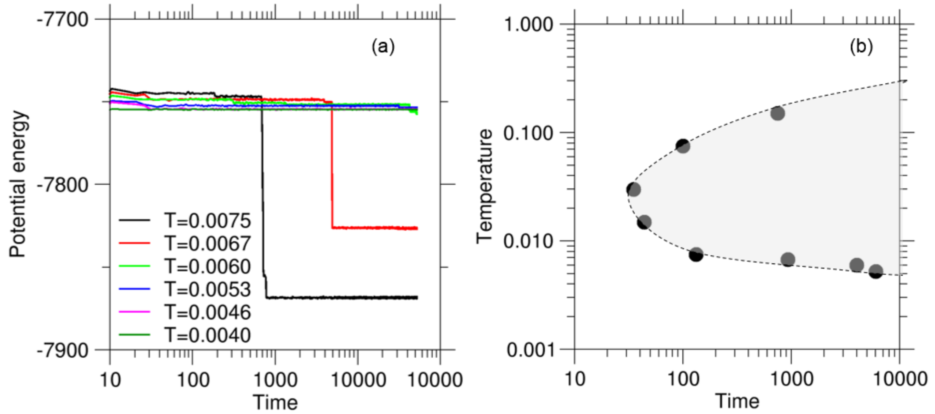

Fig. S2. Critical crystallization time for the monodisperse LJ systems. (a) Evolution of the potential energy upon crystallization under select temperatures. (b) TTT curve showing the time before crystallization occurs as the function of temperature. Reduced units are used.

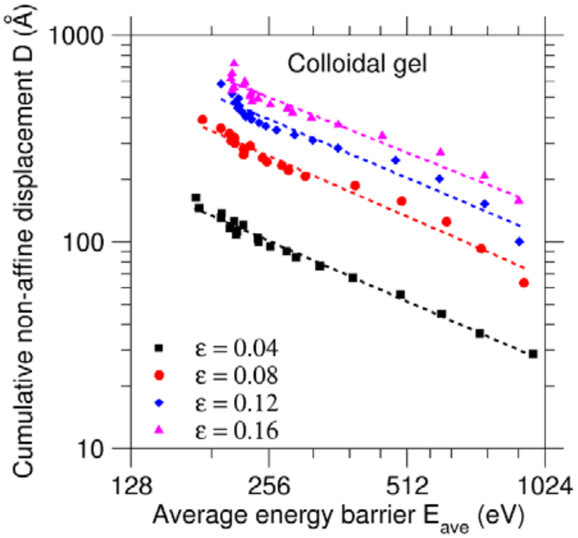

Fig. S3. The validation of power law relationship under the finite temperature. Cumulative non-affine displacements *D* of the particles during a 300 K fracture as a function of the average energy barrier that is accessible to them. The data are presented for a hydrated silicate colloidal gel characterized by a degree of disorder *s* = –0.35 subjected to different strains. The lines are some power law fits.

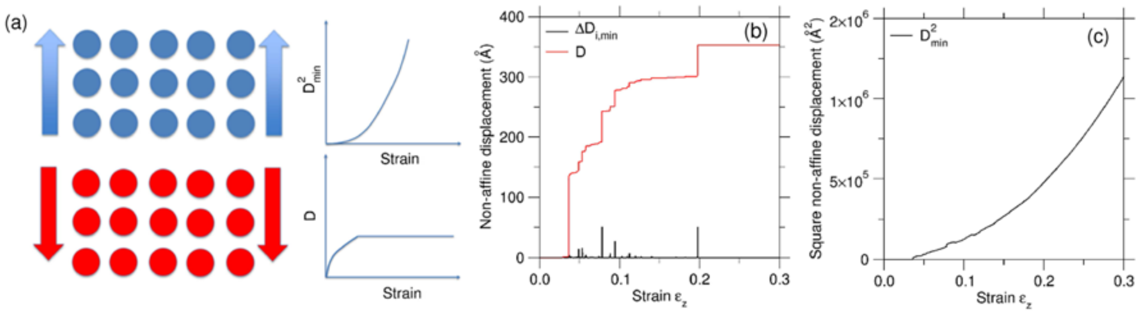

Fig. S4. Effectiveness of the cumulative non-affine displacement. (a) Schematic illustrating the difference between the conventional non-affine square displacement $D^2_{\min}$ (top plot) and the cumulative non-affine displacement *D* (used herein, bottom plot) of a single atom during the fracture process. Here, the top blue particles move upward as a rigid body, whereas the bottom red particles move downward. (b) $\Delta D_{i,\min}$, *D*, and (c) $D^2_{\min}$ of the same particle as the function of strain during the fracture process.

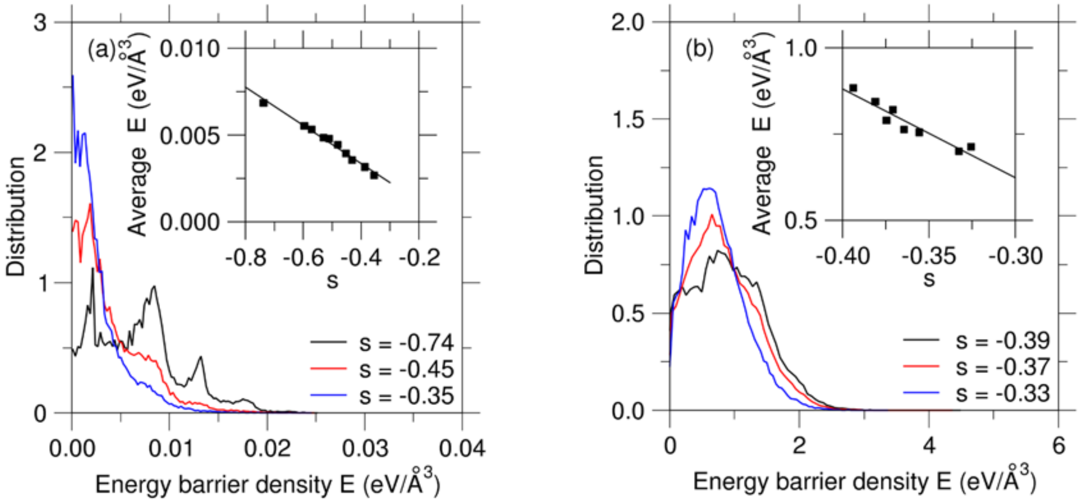

Fig. S5. Distributions of the volumetric density of energy barrier in (a) colloidal gels and (b) silica glasses with selected degrees of disorder. The energy barrier is rescaled by the cube of the interparticle distance in each system (i.e., 50 Å in the colloidal gel and 1.6 Å in glassy silica).

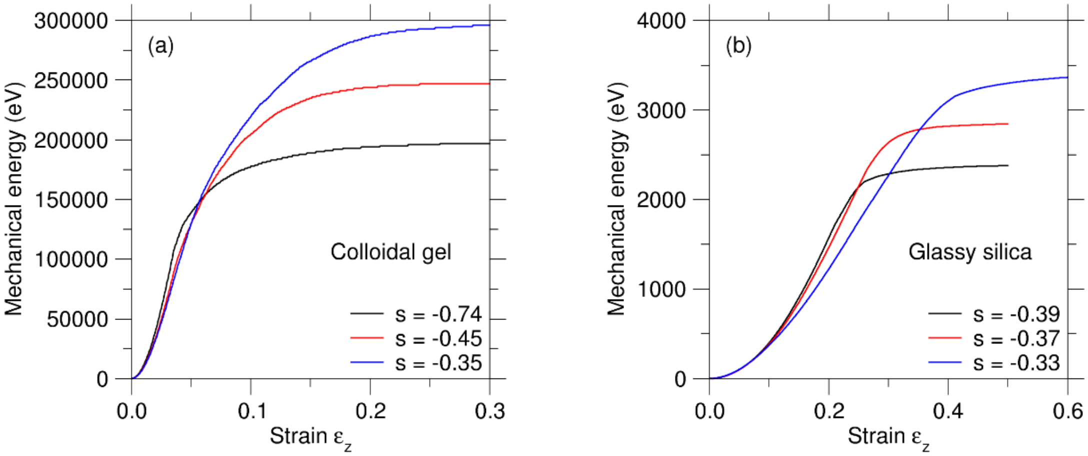

Fig. S6. Mechanical energy resulting from the imposed deformation in (a) colloidal gels and (b) silica glasses with selected degrees of disorder as the function of strain.

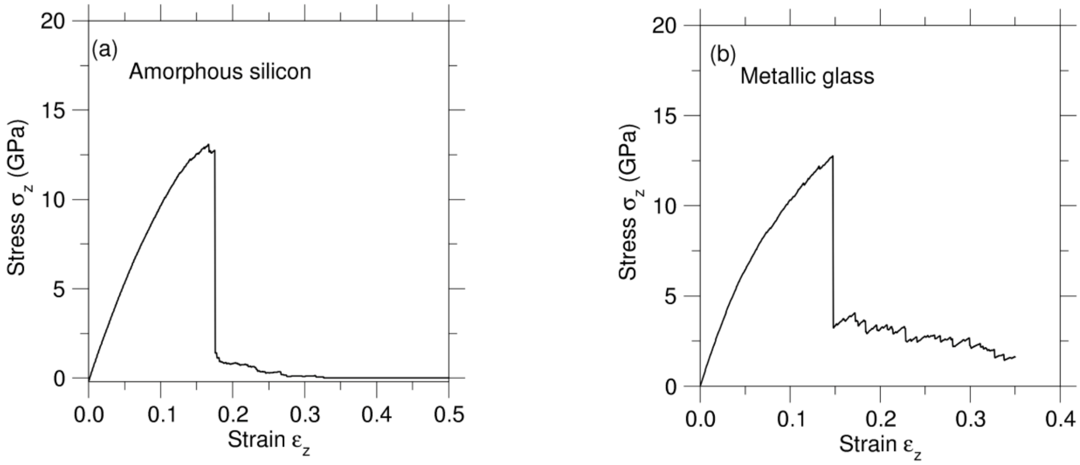

Fig. S7. Stress-strain curves of the (a) amorphous silicon and (b) metallic glass systems considered herein under uniaxial tension.

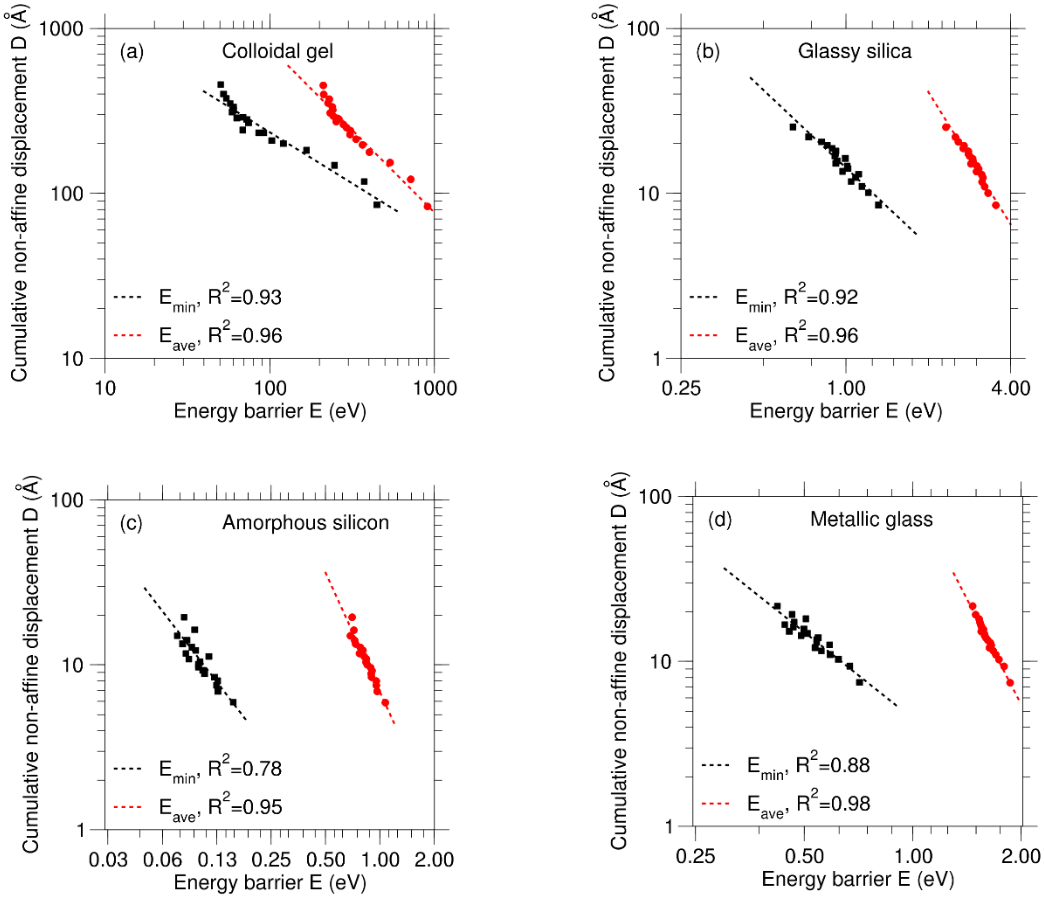

Fig. S8. Cumulative non-affine displacements *D* of the particles during fracture as a function of the average (red) and minimum (black) height of the energy barriers that are accessible to them. The dashed lines are the power law fits.

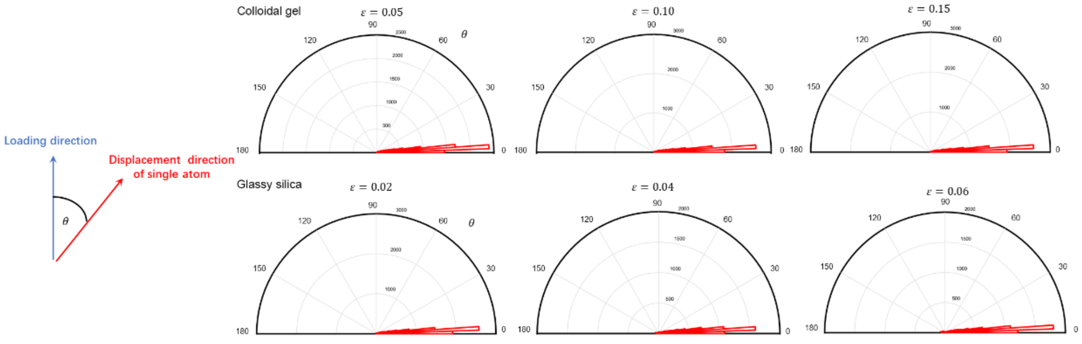

Fig. S9. Distribution of the angles between the direction of the displacements of the particles and the direction of the external load at selected strains in the colloidal gel and glassy silica systems considered herein.

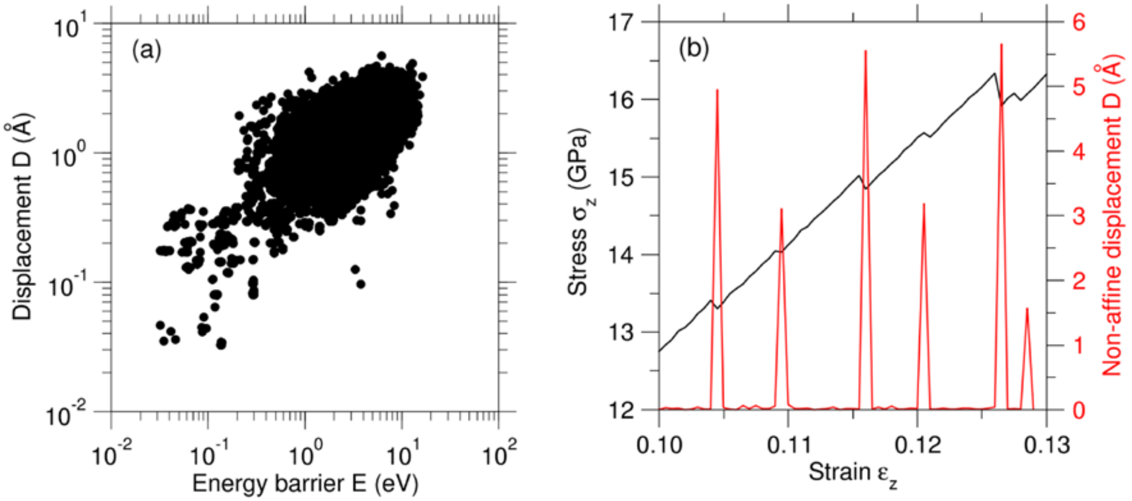

Fig. S10. Distribution of the angles between the direction of the displacements of the particles and the direction of the external load at selected strains in the colloidal gel and glassy silica systems considered herein.

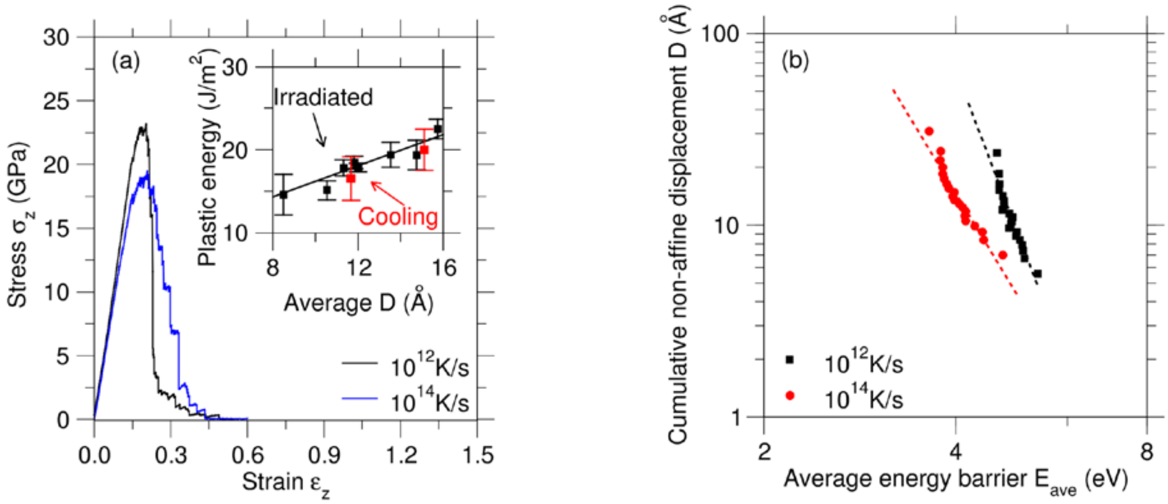

Fig. S11. (a) Stress-strain curves of select silica glasses with distinct cooling rates upon uniaxial tensile deformation. The inset shows the plastic energy dissipated during fracture as a function of the average cumulative non-affine displacements *D*. The line is to guide the eye. (b) Cumulative non-affine displacements *D* of the atoms during fracture as a function of the average height of the energy barriers that are accessible to them.